JOURNAL OF GEOPHYSICAL RESEARCH, VOL. 103, NO. B11, PAGES 27,001–27,016, NOVEMBER 10, 1998

Small-scale deformations associated with the 1992 Landers, California, earthquake mapped by synthetic aperture radar interferometry phase gradients

Evelyn J. Price and David T. Sandwell

Institute of Geophysics and Planetary Physics, Scripps Institution of Oceanography, La Jolla, California

Abstract. The Landers earthquake (M_W 7.3) occurred on June 28, 1992, and ruptured nearly 100 km of previously mapped and unmapped faults in the Mojave Desert. We use synthetic aperture radar interferometry (InSAR) to examine the cumulative surface deformation between April 24 and August 7, 1992, in a 100 x 100 km region surrounding the northern portion of the earthquake rupture. Also, we introduce a technique for manipulating SAR interferograms to extract short-wavelength displacement information. This technique involves computation and subsequent combination of interferometric phase gradient maps. The InSAR results show significant deformation signatures associated with faults, fractures, dry lake beds, and mountainous regions within 75-100 km of the main rupture. Using the phase gradient method, we are able to extract small-scale deformation patterns near the main rupture. Many of the preexisting, mapped faults within 50 km of the main rupture experienced triggered slip; these include the Old Woman, Lenwood, Johnson Valley, West Calico, and Calico Faults. The InSAR results also indicate right-lateral offsets along secondary fractures trending N-NE within the left-lateral zone of shear between the main rupture and the Johnson Valley Fault. Additionally, there are interesting interferogram fringe signatures surrounding Troy Dry Lake and Coyote Dry Lake that are related to deformation of dry lake beds.

1. Introduction

We use the technique of synthetic aperture radar interferometry (InSAR) to examine small-scale features in the deformation field associated with the Landers earthquake and Big Bear aftershock. Our study is spatially limited to a 100x100 km SAR data frame surrounding the northern portion of the surface rupture (Plate 1) and is limited by data availability to temporally integrate all deformations occurring between April 24 and August 7, 1992. While the coseismic and postseismic deformations associated with this earthquake have been studied by other workers using the InSAR technique [*Massonnet et al.*, 1993, 1994; *Zebker et al.*, 1994; *Peltzer et al.*, 1994; *Feigl et al.*, 1995; *Peltzer et al.*, 1996], our processing methods, which entail computation of phase gradients, bring out short-wavelength features to reveal previously unrecognized strain patterns.

Like the phase of an interferogram, the gradient of the phase depends on the topography and deformation of the Earth's surface and differences in the atmosphere at the two times of imaging. In an attempt to isolate the phase gradient due to deformation, the topographic contribution to the phase gradient can be computed using a digital elevation model or additional interferometric pairs and subsequently removed. Because we cannot yet remove atmospheric variations from an interferogram, we use ancillary geologic information in our interpretations of the phase and phase gradient. One of the many advantages of the phase gradient map is that it can be used to interpret large-scale interferogram phase variations by highlighting small-scale deformations on fractures and faults.

Paper number 98JB01821.
0148-0227/98/98JB-01821$09.00

The gradient of the phase is important to interferometric analysis for several reasons. First, the gradient of the phase is unique and can be computed from the real and imaginary parts of the interferogram (there are no 2π ambiguities). Second, it can be used to reduce noise in topographic interferometric measurements either through averaging of phase gradients [*Sandwell and Price*, 1997] or by aiding in the design of filters whose width is dependent on topographic slope [*Werner et al.*, 1992]. Third, the phase gradient due to topography can be subtracted from an interferogram containing phase gradient due to both topography and deformation without first unwrapping the phase. The two components of the residual phase gradient are then proportional to two components of the deformation gradient tensor rotated into a rectangular satellite coordinate system (see section 3.1): the first is proportional to the gradient of the line-of-sight (LOS) deformation in the direction of the satellite LOS (range gradient), and the second is proportional to the gradient of the LOS deformation in the direction of the satellite groundtrack.

Phase gradients attributable to deformation show small-scale variations in deformation gradient with near total coverage of the area imaged. Strain concentrations along preexisting faults and structural features are observed allowing us to study spatial heterogeneity in the deformation field of a large earthquake. This heterogeneity has been suggested by other workers to explain deviations of geodetic measurements from those predicted by elastic models [e.g., *Hudnut et al.*, 1994; *Murray et al.*, 1993]. In this paper, this heterogeneity is mapped in a SAR data frame over part of the region affected by the Landers earthquake.

1.1. Landers Earthquake Observations

The Landers earthquake sequence is conventionally characterized by three events: the April 23, 1992, 0451 UTC, 33.94°N, 116.33°W Joshua Tree earthquake (M_w 6.1); the June 28, 1992,

1158 UTC, 34.22°N, 116.43°W Landers event (M_w 7.3); and the June 28, 1992, 1507 UTC, 34.21°N, 116.83°W Big Bear event (M_w 6.2). The data discussed in this study (Table 1) contain deformation occurring between April 24 and August 7, 1992, in an area surrounding the northern part of the rupture of the Landers event (Plate 1).

The Landers earthquake has been modeled teleseismically as a two-event phenomenon with the hypocenter conventionally placed 30-40 km north of Joshua Tree as a small, shallow (3-6 km deep) M_w 6.8 earthquake with strike 359° rupturing unilaterally to the north and provoking a larger magnitude (M_w 7.15) second event about 30 km to the north having a strike of 333° [*Kanamori et al.*, 1992]. The rupture, which was initially oriented nearly due north on the Johnson Valley Fault, changed its orientation as it propagated by stepping right onto progressively more northwestwardly oriented major faults. The earthquake ruptured nearly twenty mapped and unmapped faults; the main five of which are (from south to north) the Johnson Valley Fault, the Kickapoo Fault (sometimes called the Landers Fault), the Homestead Valley Fault, the Emerson Fault, and the Camp Rock Fault (Plate 1). The maximum measured surface displacement was 5.1 m on the Emerson Fault near Bessemer Mine Road [*Hart et al.*, 1993]. In addition to the main rupture slip, triggered slip was reported on several faults within a 100 km radius including the Pisgah, Calico-West Calico (including fractures NE of Newberry Springs), Johnson Valley, upper Johnson Valley, Lenwood, Old Woman, and Pinto Mountain Faults [*Hart et al.*, 1993].

The Landers earthquake ruptured deeper and stronger than any earthquakes previously recorded in the area. It had more than 60,000 shocks including foreshocks, coshocks, and aftershocks [*Hauksson et al.*, 1993]. Shock patterns pertinent to this study include clusters of aftershocks not on the main fault rupture. In particular, aftershock clusters in our area include the Barstow sequence, a cluster near the Calico Fault north of the Mojave Valley, a cluster on the Calico Fault just east of the rupture on the Camp Rock Fault, and seismicity associated with the Newberry fractures which are northeast of the Calico Fault in the Mojave Valley [*Unruh et al.*, 1994] (Plate 1).

1.2. Regional Tectonics

The faults of the western Mojave Desert (Plate 1) define an 80 km wide region of NNW right-lateral shear and lie within the Eastern California Shear Zone (ECSZ) [*Dokka and Travis*, 1990a, b; *Savage et al.*, 1990; *Sauber et al.*, 1986]. These faults have been active since about 10.6 Ma and have accommodated 9-14% of total plate motion [*Dokka and Travis*, 1990a] at this latitude on the Pacific-North American plate boundary. The faults of the Mojave Block are characterized as discontinuous with the only fault traversing the entire length of the Mojave from the Pinto Mountain Fault to the Garlock Fault being the Calico-Blackwater system. Faults tend to end in structurally complex zones of extension or shortening with zones of extension characteristically marked by triangular-shaped lakes and zones of shortening marked by mountains and hills [*Dokka and Travis*, 1990a]. Geologically determined fault offsets show greater than 40 km of cumulative offset throughout the region south of Barstow [*Dokka and Travis*, 1990a], while geodetic results show most of the deformation in this region accommodated between the Helendale and Calico Faults south of Barstow (6.7 mm/yr) with negligible deformation to the east [*Sauber et al.*, 1986]. This contrast between geologic and geodetic results points to a recent westward migration of strain [*Sauber et al.*, 1986].

In spite of the surface rupture and shock characteristics of large earthquake swarms (April 10, 1947, Manix [*Richter*, 1947; *Doser*, 1990]; June 1, 1975, Galway Lake [*Hill and Beeby*, 1977; *Fuis and Lindh*, 1979]; and March 15, 1979, Homestead Valley [*Hill et al.*, 1980]) which have implied significant fault interactions, geologic results have led to block models of faulting in the Mojave with faults accommodating motion independently of each other in time and space [*Garfunkel*, 1974; *Carter et al.*, 1987; *Dokka and Travis*, 1990a]. These presumptions about the nature of faulting in the Mojave have led to underestimation of the earthquake magnitude potential in the area [e.g., *Wesnousky*, 1986; *Hart et al.*, 1993] and confusion as to the link between the San Andreas Fault (SAF) and the more northern parts of the ECSZ. The Landers earthquake changed these presumptions by rupturing along several faults across areas previously modeled as coherent blocks [*Hart et al.*, 1993].

1.3. SAR and InSAR

We use radar imagery data (Table 1) collected by the C-band (5.2 GHz) SAR instruments aboard the ERS-1 and ERS-2 satellites. The raw signal data are processed using a Jet Propulsion Laboratory (JPL) heritage SAR processor whose output consists of a complex signal that is a measure of the complex backscatter of a patch on the ground delayed by the travel time of the signal from sensor to target and back [see *Curlander and McDonough*, 1991; *McDonough et al.*, 1985]. After processing, the phase of a SAR image resolution element is the sum of several components: (1) the phase delay due to the two-way travel time between sensor and target (location of a SAR pixel on the ground), (2) a random phase component due to the complicated interference pattern produced by radar signal interaction with multiple ground scatterers within an image resolution element, and (3) additive noise.

InSAR is a method by which the phase differences of two SAR images are used to calculate the differences in range from two SAR antennae having slightly different viewing geometries to targets on the ground [*Graham*, 1974; *Zebker and Goldstein*, 1986] (Figures A1 and A2). The ERS radar interferometer is composed of either the same antenna on one platform "repeating" its orbit (e.g., ERS-1) or two antennae on different platforms having nearly the same orbit (e.g., ERS-1/ERS-2 tandem mission). The antennae are separated in both space and time (repeat-pass interferometry), and range differences can be due to a number of sources including topography, surface deformation, and atmospheric differences at the two times of imaging. The

Table 1. Data Frames and Baseline Parameters Used in this Study

Reference		Repeat		Baseline	
Satellite: Orbit_Frame	Acquisition Date	Satellite: Orbit_Frame	Acquisition Date	Length, m	Elevation Angle, α
ERS1: 5554_2907	Aug. 7, 1992	ERS1: 4051_2907	April 24, 1992	147.1	152.4
ERS1: 22932_2907	Dec. 3, 1995	ERS2: 3259_2907	Dec. 4, 1995	105.7	178.6
ERS1: 23433_2907	Jan. 7, 1996	ERS2: 3760_2907	Jan. 8, 1996	137.0	178.4

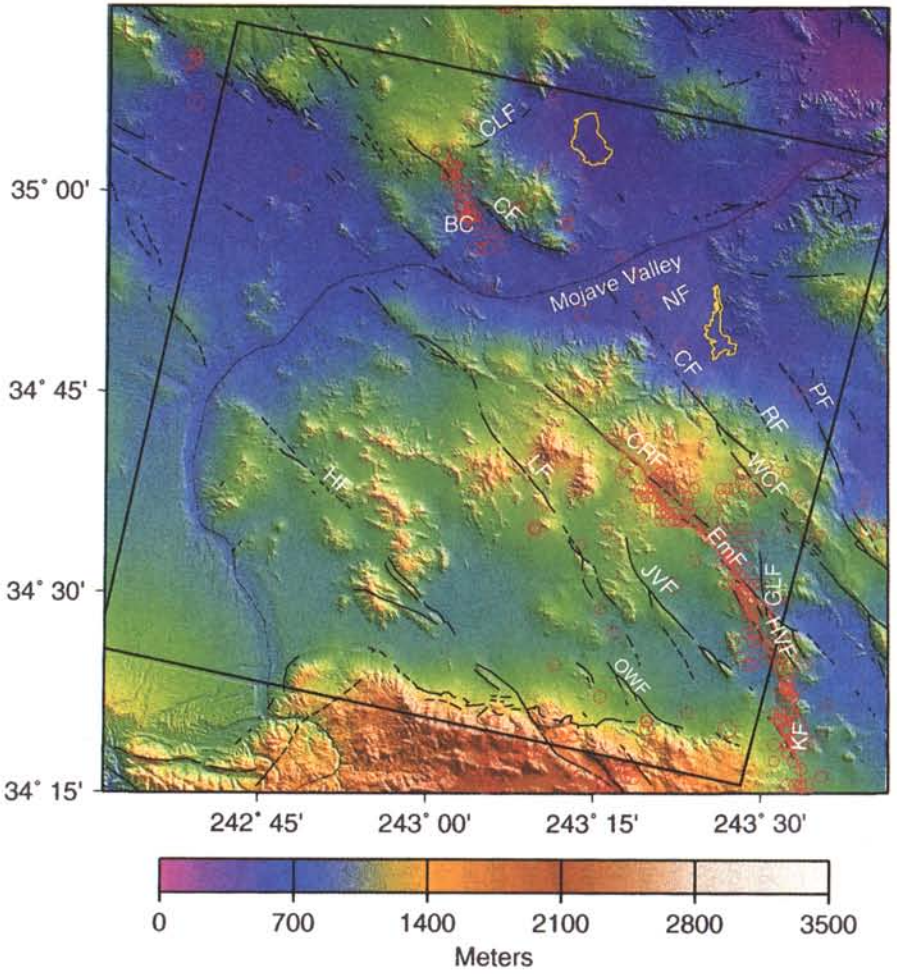

Plate 1. The 60 m digital elevation model (DEM) of the study area derived from InSAR and U.S. Geological Survey (USGS) 1° DEM. Shocks with $M > 3.0$ (circles and stars) occurring between April 24 and August 7, 1992, are plotted. Stars show shocks at the intersection of the Barstow earthquake cluster and the Calico Fault. The box indicates the position of the SAR imagery. Abbreviations are Helendale Fault (HF), Old Woman Fault (OWF), Lenwood Fault (LF), Johnson Valley Fault (JVF), Emerson Fault (EmF), Camp Rock Fault (CRF), Galway Lake Fault (GLF), West Calico Fault (WCF), Calico Fault (CF), Rodman Fault (RF), Pisgah Fault (PF), and Coyote Lake Fault (CLF). Five bench marks are plotted: Rock (ROK), Fry (FRY), Old Woman (OWN), Boulder (BDR), and Means (MNS).

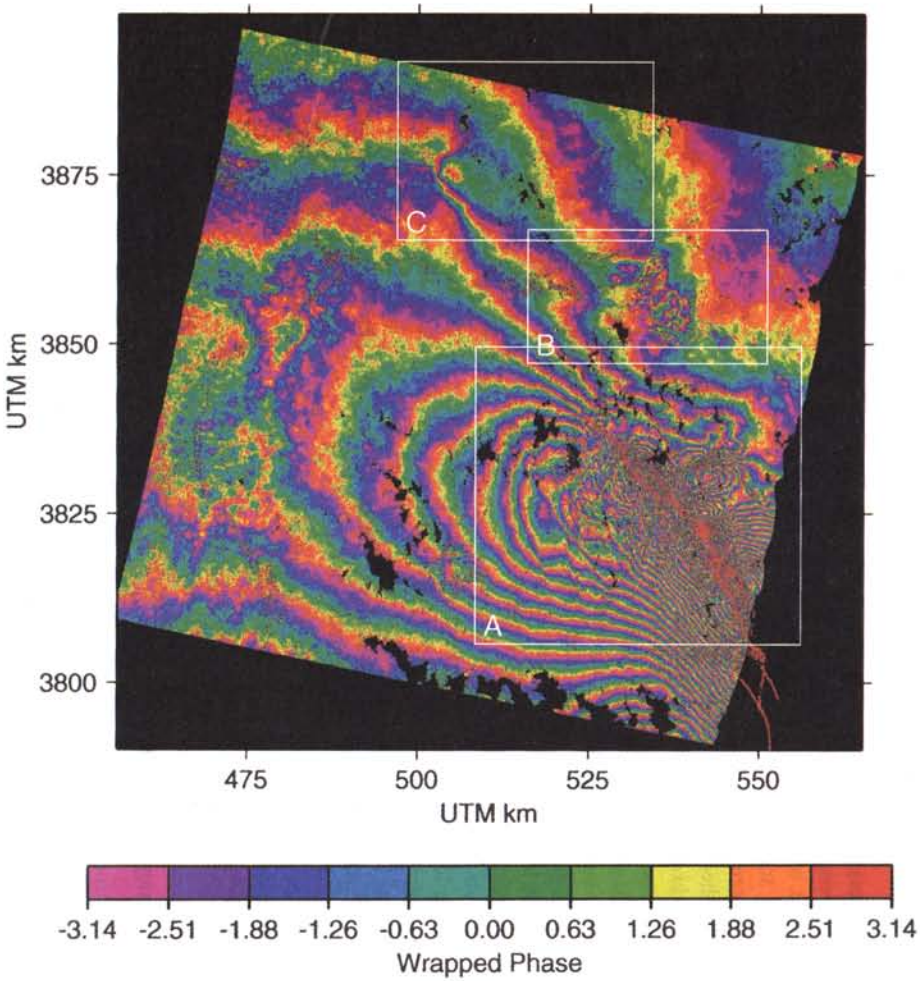

Plate 2. Interferogram deformation fringe phase. Boxes show areas A, B, and C which are discussed in the text. Red lines are field mapped earthquake rupture [*Sieh et al.*, 1993].

line that connects the two antennae in space is called the interferometer baseline (Figures A1 and A2).

In repeat-pass interferometry, spatial coverage limitations are imposed by phase decorrelation and the geometry of imaging. Three sources of phase decorrelation have been identified as temporal decorrelation due to motion of scatterers between imaging times, spatial decorrelation that is more influential when the interferometric baseline is longer, and thermal noise in the system electronics [*Goldstein et al.*, 1988; *Zebker and Villasenor*, 1992]. In areas of complete spatial or temporal decorrelation (very steep topography or the area surrounding the Landers surface rupture, respectively), the phase cannot be recovered. The sensor's ability to image the terrain with geometric fidelity depends on the slope of the terrain and the look angle of the radar. "Robust" imaging of the terrain can occur only if the slope does not satisfy the criteria for geometric layover or shadowing. Because ERS-1/ERS-2 have a steep average look angle of 21°, geometric layover is a common phenomenon in mountainous areas. The black patches in Figure 2 and Plates 2-5 occur in areas where the topographic interferogram could not be unwrapped using a "tree" algorithm [e.g., *Goldstein et al.*, 1988]. They exist in the phase gradient map (which should show total coverage) because we used the topography computed from the topographic interferogram to perform orthorectification on our images.

1.4. Effects of Propagation Medium on Range Delay

Because we cannot yet remove the atmospheric signal from the topographic phase-corrected interferograms, it is important to be able to recognize atmospheric artifacts in interferograms so they are not confused with tectonic deformations. Short-wavelength atmospheric artifacts (which could be confused with small-scale tectonic deformations) typically have length scales of the order of 5-10 km and can cause as much as 10 cm of excess two-way path length (three interferogram fringes). Examples are given by *Massonnet and Feigl* [1995a], *Rosen et al.* [1996], and *Zebker et al.* [1997].

Regional atmospheric effects corresponding to long-wavelength ionospheric perturbations, and differences in the hydrostatic component of the troposphere manifest themselves as a planar phase trend in an interferogram [*Tarayre and Massonnet*, 1996]. This phase trend makes it necessary either to compute an "artificial baseline" [*Tarayre and Massonnet*, 1996] or to remove the long-wavelength atmospheric effect from the interferogram at some point in the data processing. If these regional effects are not removed, they will produce a constant offset in the phase gradient map which could be interpreted as a regional tilt.

Despite variations in the refractivity of the atmosphere and ionosphere, repeat-pass InSAR has proved valuable for applications involving deformation of the surface of the Earth. Several studies [*Zebker et al.*, 1994; *Massonnet et al.*, 1993] have compared coseismic deformation signatures obtained from InSAR with those measured by Global Positioning System (GPS). *Zebker et al.* [1994] found the correlation of GPS displacements with those obtained from his interferometric method to be 0.958, while *Massonnet et al.* [1993] found interferometric displacement estimates to agree with GPS measurements of displacement within 3.4 cm RMS. Also, the results of forward modeling of the large-scale ground displacement field near earthquakes agree qualitatively with InSAR fringe maps [*Massonnet et al.*, 1993; *Peltzer et al.*, 1994]. In this study, we differentiate between small, localized tectonic deformations and atmospheric artifacts using proximity to pre-existing geologic structures as a discriminative criterion.

2. Data Processing

The basic steps of our InSAR data processing are quite standard. We process the raw radar echoes to SAR images and match the images to a subpixel level. We then form an interferogram by multiplying each complex pixel in one image by the complex conjugate of the matching pixel in the other image. Interferograms computed in this fashion have a corrugated appearance [*Li and Goldstein*, 1990, Figure 7] resulting from a high phase rate in range due to imaging geometry. The flat Earth correction (Appendix A) [*Zebker et al.*, 1994] removes those fringes due to Earth curvature and imaging geometry.

There are some data processing steps that are either done differently here than in previous studies or should be elaborated upon for the sake of explaining the resolution and interpretation of our results. These include estimation of baselines from orbital knowledge, image filtering, and phase gradient computation and combination.

2.1. Estimation of Interferometer Baselines From Orbital Knowledge

In contrast to previous studies, which estimated baseline parameters from imagery and topography data, we computed baselines from ERS-1/ERS-2 precise orbits provided by *Scharroo and Visser* [1998] (Table 1). These orbits have radial accuracies of 50 mm and crossover repeatability within 70 mm, giving an overall baseline accuracy better than 70 mm. The advantage of this approach is that surface displacements and long-wavelength atmospheric artifacts are not absorbed into the baseline estimate. Repeat orbits are usually not parallel, necessitating the computation of a new baseline at several points in azimuth within an image frame [e.g., *Gabriel and Goldstein*, 1988].

Let $\mathbf{s}(t_1)$ be the vector position of the satellite at time t_1 within the timespan of the reference frame. We search the orbit over the timespan of the repeat frame for time t_2, the time of closest approach. If $\mathbf{s}(t_2)$ is then the vector position of the satellite within the timespan of the repeat frame, the total baseline length is

$$B = |\mathbf{s}(t_2) - \mathbf{s}(t_1)| \tag{1}$$

and the baseline elevation angle (α) is

$$\alpha = \tan^{-1}\left(\frac{B_V}{B_H}\right) \tag{2}$$

where B_V and B_H are the local vertical and horizontal components, respectively, of the baseline:

$$B_V = (\mathbf{s}_2 - \mathbf{s}_1)\cdot\frac{\mathbf{s}_1}{|\mathbf{s}_1|} \tag{3a}$$

$$B_H = \pm\left(B^2 - B_V^2\right)^{1/2} \tag{3b}$$

The sign of the horizontal component is positive in the direction of radar look.

2.2. Interferogram Filtering

Methods of filtering interferograms range from simple averaging over pixels (taking looks) [e.g., *Gabriel et al.*, 1989] to

spatially variable filters whose power spectra are matched to that of the local phase [*Goldstein et al.*, 1988; *Werner et al.*, 1992]. We filtered the real and imaginary parts of the complex interferogram (with pixel spacing as sampled by the radar) separately using a low-pass Gaussian 5 point by 17 point filter whose characteristics are discussed in Appendix B. Because none of the baselines of the interferograms examined in this study are longer than 150 m, we do not find in necessary to use an adaptive filter.

2.3. Phase Gradient Computation

Analysis of the phase gradient image is a new approach to studying small-scale surface deformation. The gradient of the interferogram phase is computed directly from the real and imaginary parts of an interferogram and is scaleable by any real number, whereas the phase of an interferogram, measured modulo 2π, can only be scaled by an integer. The expression for the phase gradient ($\nabla\phi$) of a complex interferogram is

$$\nabla\phi(x) = \frac{R\nabla I - I\nabla R}{R^2 + I^2} \tag{4}$$

where R and I are the real and imaginary parts, respectively, of the interferogram and ∇ denotes a gradient operator. This expression is equivalent to one obtained by *Werner et al.*, [1992], but differentiation is performed in the spatial domain rather than the frequency domain.

Averaging of phase gradient images, or stacking, to produce a topographic phase gradient model is useful for decreasing the noise level of the data and averaging out atmospheric range errors [*Sandwell and Price*, 1997]. Before phase gradients can be stacked, they must be scaled to some common baseline. This is done using a scale factor that is equal to the ratio of the perpendicular baselines after the flat Earth correction (Appendix A) has been applied [e.g., *Zebker et al.*, 1994]. The expression for the average phase gradient from N interferograms each having scale factor b_i (see Appendix A) is

$$\overline{\nabla\phi} = \frac{1}{N}\sum_{i-1}^{N} b_i \nabla\phi_i \tag{5}$$

In this study, we averaged two pairs from the ERS-1/ERS-2 tandem mission to obtain an estimate for the topographic phase gradient. We then scaled and subtracted this topographic phase gradient from the interferogram phase gradient for the ERS-1 pair which includes the earthquake (Table 1) to obtain an estimate of the phase gradient (Figure 2) related to the deformation which occurred between April 24 and August 7, 1992.

3. Interferogram Interpretation and Transformation of Displacement and Deformation Gradient Into the Satellite Reference Frame

The quantity that relates deformations and topography to InSAR geometry (Figure A2) is the difference in range to a point on the ground between repeat and reference passes of the satellite ($\delta\rho$). This change in range is related to the interferometric phase (ϕ) by

$$\phi = \phi_2 - \phi_1 = \frac{4\pi}{\lambda}\delta\rho \tag{6}$$

where ϕ_1 is the phase of a pixel in the reference image, ϕ_2 is the phase of a pixel in the repeat image, and ρ is the range from the satellite to the target during the satellite's reference pass.

If deformation has occurred between the two times of imaging, ϕ is proportional to the sum of a geometric (flat Earth) $\delta\rho_e$, a topographic $\delta\rho_t$, and a deformation $\delta\rho_d$ contribution to the range change [*Zebker et al.*, 1994] (Appendix A)

$$\phi = \frac{4\pi}{\lambda}\left(\delta\rho_e + \delta\rho_t + \delta\rho_d\right) \tag{7}$$

When the topographic and geometric phase contributions are removed, the residual phase can be assumed to be due to deformation and is

$$\phi = \frac{4\pi}{\lambda}\delta\rho_d \tag{8}$$

where $\delta\rho_d$ is the magnitude of the displacement in the direction of the satellite LOS. Each fringe in Plates 2 and 3b-5b represents 2.8 cm of displacement in the satellite LOS direction.

The geometric relationship between an Earth-based rectangular coordinate system and a satellite referenced system is illustrated in Figure 1. Assuming that the radar LOS and satellite groundtrack directions are orthogonal, we define a right-handed rectangular coordinate system in the satellite reference frame in which the directions of the first, second, and third rectangular vector components are in the satellite LOS direction, the satellite

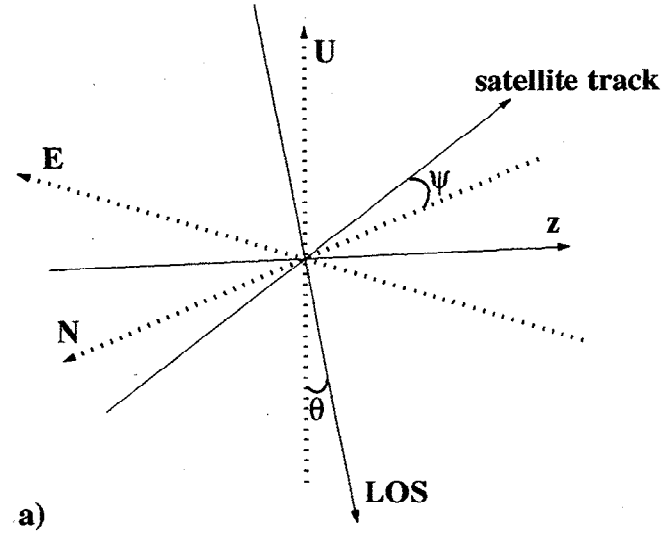

a)

	LOS	Satellite Track	z
E	-sinθ cosψ	sinψ	-cosθ cosψ
N	sinθ sinψ	-cosψ	cosθ sinψ
U	-cosθ	0	sinθ

b)

Figure 1. (a) Rectangular coordinate systems for Earth-based geometry (E, N, U) and satellite-based geometry (LOS, satellite track, z); θ is the look angle of the radar, and θ is the angle between the satellite track and south. (b) Rotation matrix to transform Earth-based coordinates into satellite-based coordinates.

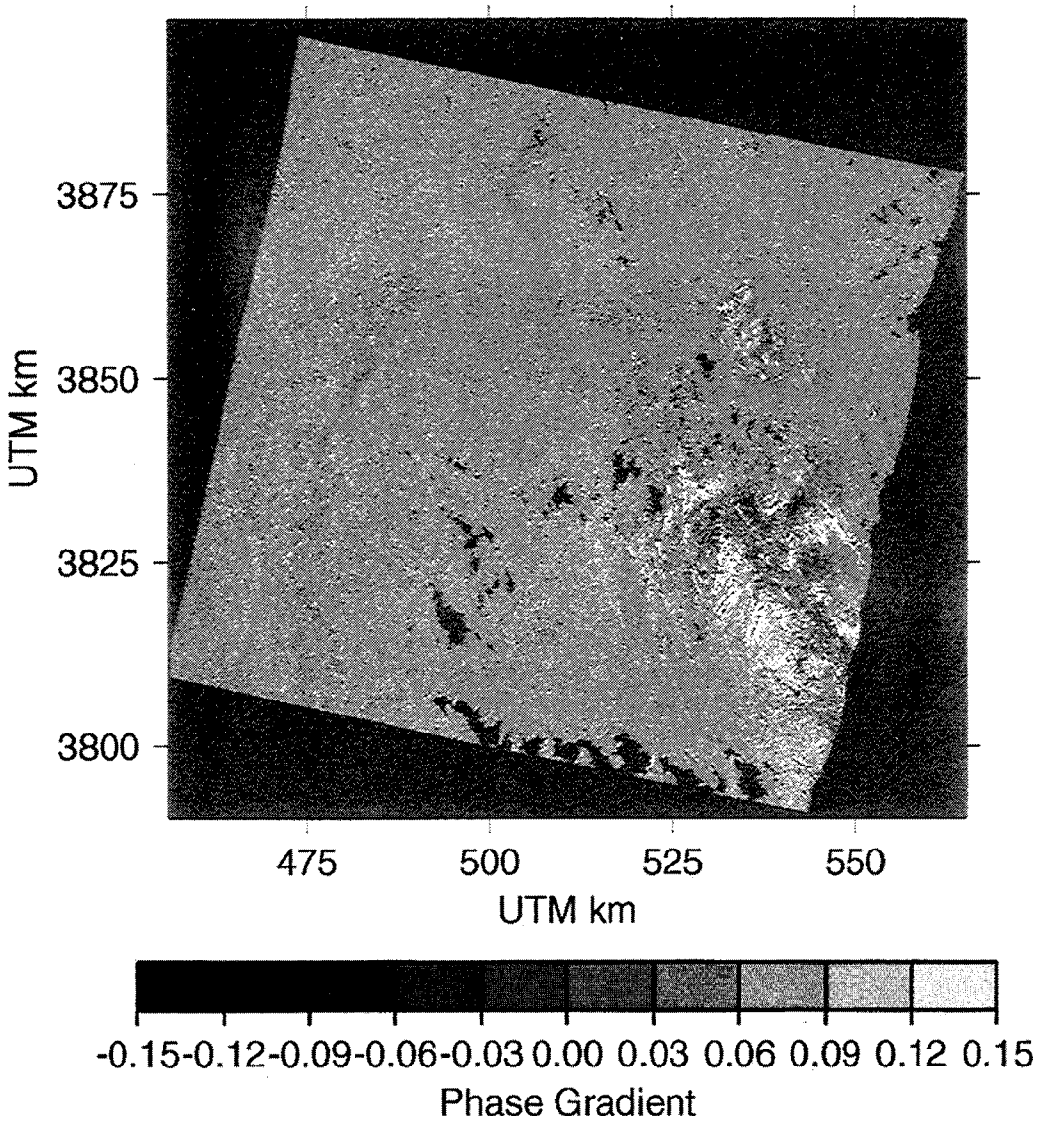

Figure 2. Interferogram deformation phase gradient formed by subtracting scaled topographic phase gradient from April 24 to August 7, 1992, interferogram phase gradient.

along-track direction, and the direction perpendicular to the plane of imaging (z), respectively. We then find the rotation matrix (**A**) that transforms Earth-based rectangular coordinates (east (E), north (N), up (U)) into the satellite coordinate system. The rotation matrix **A** is fully determined (for a descending pass geometry) by defining the along-track axis to lie in the Earth-referenced E-N plane and to make an angle of 180°-ψ with the N axis (where ψ is the angle between the satellite groundtrack and south), the LOS axis to make an angle 180°-θ with the U direction (where θ is the radar look angle), and the base vector perpendicular to the plane of imaging to make an angle 90°-θ with the U direction (Plate 2). The assumption that the LOS and along-track directions are orthogonal is reasonable in our case since the angle between them (in the imaging plane) is 90° $\pm \sigma$, where σ, the squint angle, is less than 0.03° for the ERS imaging radars.

If $\underline{\mathbf{u}}$ is the displacement in the satellite coordinate system and $\mathbf{u}$ is the displacement in the Earth-based coordinate system,

$$\underline{\mathbf{u}} = \mathbf{A}\mathbf{u} \tag{9}$$

and the displacement measured by the radar interferometer is the LOS component of $\underline{\mathbf{u}}$ which is $\underline{u}_1$.

The gradient of the displacement in the Earth-based coordinate system can be transformed using the same rotation matrix to yield tensor components proportional to the phase gradient of deformation. If the deformation gradient tensor [e.g., *Malvern*, 1969] in the Earth-based coordinate system is $\mathbf{J}$ and the deformation gradient tensor in the satellite coordinate system is $\underline{\mathbf{J}}$, then

$$\underline{\mathbf{J}} = \mathbf{A}\mathbf{J}\mathbf{A}^{\mathrm{T}} \tag{10}$$

The two components of phase gradient due to deformation that we can measure using InSAR are proportional to two components of $\underline{\mathbf{J}}$: $\underline{J}_{11}$ is the derivative of $\underline{u}_1$ in the LOS direction, and $\underline{J}_{12}$ is the derivative of $\underline{u}_1$ in the along-track direction. Our phase gradient maps plot only the deformation gradient component that is in the LOS direction because this component highlights the predominantly N-S structures. Note that the deformation gradient tensor includes both strain and rotation.

As is evident from this analysis, the LOS component of deformation is a linear combination of all the components of the Earth-referenced deformation as are the two phase gradient components a linear combination of all the deformation gradient components in an Earth-based coordinate system. Because of this, other information including geologic mapping, GPS measurements, earthquake orientations, and/or assumptions about the nature of the deformation is necessary to interpret radar interferometric measurements. Even in the case where ascending and descending passes of the satellite are available for a given deformation event, information about the magnitude of the horizontal displacement vector or its orientation is necessary to determine its three components.

The phase gradient presented in Figure 2 and Plates 3a-5a, is capable of both adding to the knowledge about the earthquake rupture pattern and mapping extensions of faults difficult to trace geologically by highlighting strain concentrations on secondary fractures and triggered or sympathetic slip on major faults. The larger-scale deformation patterns are best observed as variations in the wrapped phase since their contribution to the phase gradient measurements is that of a regional constant shift.

4. Results

The stacked LOS phase gradient (equation (5)) of two ERS-1/ ERS-2 tandem mission interferograms was scaled and subtracted from the phase gradient of the ERS-1 April 24 to August 7, 1992, interferogram to produce the gradients shown in Figure 2 and Plates 3a-5a. The unwrapped phase of the December 3-4, 1995, tandem interferogram was scaled and subtracted from the phase of the April-August 1992 interferogram to produce the fringes in Plates 2, 3b-5b. Because each image was collected during a descending pass of the right-looking ERS satellite, the nearest range to the satellite is on the right-hand side of the figures.

Plate 2 and Figure 2 show the relationship of the deformation phase gradient to the deformation fringe phase for the entire area of the study (100 km by 100 km) defined by an ERS data frame. The deformation fringe phase is comparable to maps shown in other studies [*Massonnet et al.*, 1993; *Zebker et al.*, 1994]. The most obvious feature in the map is the region of phase decorrelation around the main rupture. Ground scatterers in this region underwent random motions between the two imaging times with length scales greater than the wavelength of the SAR. The phase cannot be recovered here. Three areas outside the decorrelated rupture signature show remarkable deformation fringe and phase gradient signatures. Area A (Plate 3) surrounds the end of the rupture and includes the Camp Rock (CRF), Emerson (EmF), Johnson Valley (JVF), and Lenwood (LF) Faults and small parts of the Calico Fault (CF). Area B (Plate 4) includes the Calico and Pisgah (PF) Faults as they traverse the latitude of the Mojave Valley (MV) as well as deformation related to structures which have been dubbed the Newberry fractures [*Unruh et al.*, 1994]. Area C (Plate 5) includes Coyote Dry Lake (CDL) and the Barstow earthquake cluster [*Hauksson et al.*, 1993].

4.1. End of the Main Rupture

The fringe pattern between the Johnson Valley Fault and the main rupture is dense and elongated parallel to the azimuth of the rupture (Plate 3b). The density of fringes decreases logarithmically across the Johnson Valley from east to west as is expected from elastic half-space modeling of the lithosphere [see *Massonnet et al.*, 1993]. Because of the viewing geometry mentioned above, this pattern is indicative of either a left-lateral shear in the direction of earthquake rupture or a tilt of the region between the Camp Rock-Emerson and Johnson Valley Faults. Between the Camp Rock-Emerson and Johnson Valley Faults, negative phase gradients occur in linear patterns striking N-NE (Plate 3a). It is likely that these correspond to secondary fault rupture at depth. The fringes across these secondary faults ramp downward with increasing range, indicating relative ground movement away from the satellite on the western sides of the faults. If no vertical deformation is assumed, this evidence, combined with the observation of negative phase gradients and the orientations of the fractures, indicates left-lateral displacements across these secondary structures. Offsets along each of the secondary faults between the Johnson Valley Fault and the main rupture are typically 2 rad which is equivalent to 9 mm of LOS displacement.

The elongated fringe pattern in the upper Johnson Valley is limited to the north by an arcuate feature seen in the phase gradient map (Plate 3a) which defines the transition of the surface morphology from alluvial fill to mountainous. This feature demarcates the northern extension of the Fry Mountains (area marked B in Plate 3a) and is one of the bounds on a zone a complex deformation [*Zebker et al.*, 1994, Plate 6, area B] that extends west to the Ord Mountains, north to the rupture on the Camp Rock Fault, and south to the Fry Mountains. Although previous workers have interpreted this region to contain "cracking" [*Zebker et al.*, 1994], analysis of the azimuth and range gradient maps indicates drainage patterns intersecting a fracturing pattern consistent with the style of deformation in the upper Johnson Valley. While geologic maps [*Dibblee*, 1964] of the area show the termination of the Johnson Valley Fault near its intersection with the Fry Mountains, the interferometric phase gradient shows an offset along a fracture connecting the mapped terminus of the Johnson Valley Fault with the Camp Rock Fault near the terminus of the earthquake rupture (Plates 3a and 3c). This linkage is not obvious in the fringe map (Plate 3b). This extension of the Johnson Valley Fault is the only coherent feature within the zone of complex deformation. Geologic mapping results show an east-side-down offset along a short fracture intersecting the end of the rupture on the Camp Rock Fault near GPS site 7000 (Plate 3c) that may correspond to this northward extension of the Johnson Valley Fault (K. LaJoie, personal communication, 1997).

While the northern end of the Fry Mountains intersects the main rupture trace, from the west, at the north end of the step-over region linking the Emerson Fault and the Camp Rock Fault, the south end of the step-over region is flanked to the east by a northeastwardly trending Mesozoic structure called Iron Ridge (Plate 3c). After the earthquake, two NE to east striking zones of aftershocks bordered Iron Ridge to the north and south (Plate 1) [*Hauksson et al.*, 1993]. The northern zone of aftershocks is associated with triggered slip on left-lateral, NE striking fractures [*Hart et al.*, 1993; K. LaJoie, personal communication, 1997].

Iron Ridge corresponds directly to a region of rounded, nearly circularly enclosed fringes in the interferogram (Plate 3b, label C). Fringes ramp upward to the west with positive phase gradient on the satellite side of Iron Ridge and ramp downward to the west with negative phase gradient on the opposite side. The semicircular fringes are most likely indicative of uplift during the time period surrounding the earthquake with the central fringe representing maximum displacement toward the satellite. The phase variation across this feature is 37.5 rad representing 16.8 cm of

LOS displacement. The zone of semicircular fringes is cut to the northeast by the West Calico Fault (WCF) (Plate 1) and bounded farther to the east by a southeastward extension of the Calico Fault as evidenced in the interferometric phase gradient map (Figure 5a) and previously mapped fault locations (Plate 3c).

The phase gradient is positive along linear features (Plate 3c, label D) located southwest of the Johnson Valley which correspond to the Lenwood Fault, a northern extension of the Old Woman Fault, and an unidentified fault west of the Old Woman Fault (Plate 3c). The fringe map exhibits upward ramping of fringes across these structures from east to west indicating relative displacement toward the satellite on the west sides of the faults. LOS displacements across the faults are typically 15 mm. If the displacement across these faults was purely horizontal, the phase gradient features and fringe patterns indicate left-lateral sympathetic slip. If the displacement is vertical, there was uplift on the west sides of these faults relative to the east sides.

4.2. Calico Fault and Newberry Fractures

The Calico Fault (Plates 1 and 4) runs beneath the Mojave Valley in the left half of Plate 4. The phase gradient is negative along this fault while the deformation fringe phase shows downramping from east to west, indicating relative displacement away from the satellite on the west side of the fault. A strain concentration on this fault is not obvious in the fringe map. The LOS displacement across this fault is 8-9 mm. Assuming only horizontal offset, the interferometric evidence suggests that the offset was right-lateral. This agrees with mapping results reported by *Hart et al.* [1993].

The fractures in the center of Plate 4 have been mapped and named the Newberry fractures [*Unruh et al.*, 1994; K. LaJoie, personal communication, 1997]. Geologic mapping shows that they are purely extensional in a NE-SW direction. LOS displacements across the fractures range from 5 to 22 mm. Associated with these fractures, the interferometry results show two regions of enclosed fringe patterns. A relative LOS displacement of 13 mm is present across the northern fringe pattern, while a relative LOS displacement of 44 mm is present across the southern fringe pattern. The interferogram fringes ramp down toward the centers of the patterns, and the phase gradients are negative on the satellite sides of the fringe patterns and positive on the sides farther from the satellite. Because of their association with the extensional Newberry fractures and their location near Troy Dry Lake, the ground features are here interpreted as subsidence basins.

4.3. Barstow Aftershock Cluster and Coyote Lake

The Barstow earthquake cluster trended north to northwest (Plates 1 and 5b) and did not occur on known surface faults. The maximum magnitude earthquake in the cluster occurred on August 5, 1992 [*Hauksson et al.*, 1993], with magnitude 4.7 (Council of the National Seismic System (CNSS) earthquake database). The fringe pattern in the left-hand portion of Plate 5 consisting of two, coupled bull's-eyes (one positive LOS displacement and one negative LOS displacement) straddles the intersection of the Barstow cluster, the Calico Fault and the Coyote Lake Fault (Plate 5c). Several earthquakes with magnitude greater than 3.5 occurred at or near this location during the time period between April 24 and August 7, 1992 (Plates 1 and 5b; stars). The phase gradient image shows little indication of a surface fault rupture. The fringes indicate right-lateral offset across the Calico Fault with vertical uplift of the Calico Mountains, or left-lateral offset across the conjugate Coyote Lake Fault. The shocks in the Barstow cluster had a predominantly right-lateral, strike-slip focal mechanism [*Hauksson et al.*, 1993]. The relative LOS displacement measured across the enclosed fringes is 5.3 cm.

Flanking the east side of the Calico Mountains, a structure which may be a northeastern branch of the Calico Fault is apparent in the phase gradient map (Plate 5a, label C; Plate 5c). The fault appears to include a series of right-lateral strike-slip offsets connected by extensional cracks. This is evidenced by the change in phase gradient signature from negative to a negative-positive double as the fracture changes orientation. Typical LOS displacements of 5 mm are associated with right-lateral offsets across this fault.

Northeast of this apparent northeastern branch of the Calico Fault is Coyote Dry Lake (Plate 5a, label D; Plate 5c). The deformation fringe phase and phase gradient maps show deformation of the lake shore between the time period April 24 and August 7, 1992, and a small amount of what can be interpreted as subsidence within the lake bed itself. Subsidence in the interior of the lake bed was 9-10 mm LOS, while deformation along the shoreline reached 13 mm LOS across some features. This deformation could be either earthquake related or indicate a seasonal change of the lakebed between spring and summer.

5. Discussion

The interferometric results presented here indicate that small-scale LOS deformations associated with the Landers earthquake occurred within 75-100 km of the main rupture. These small-scale deformations are superimposed on a deformation field such as might be expected from the response of an elastic lithosphere to the Landers earthquake [e.g., *Massonnet et al.*, 1993, Figure 3b]. These small-scale deformations are associated with secondary fractures, preexisting faults, dry lake beds, and mountainous regions; they provide insight into the formation of such geomorphic features and help define the role of these features in fault interactions. Furthermore, interferometric maps showing small-scale deformations could be used as a reconnaissance tool for mapping faults and coseismic displacements and for decisions involving GPS receiver location or GPS data exclusion from inversions that assume elastic behavior.

The long, linear secondary faults superimposed on the dense, elongated fringe pattern between the Johnson Valley Fault and the main rupture (Plate 3) indicates a shear zone between the main rupture trace and the Johnson Valley Fault with probable faulting of the basement rock. Faulting is believed to extend to the basement because it is unlikely that the overlying alluvium is cohesive enough to sustain fractures with lengths of 10 km. Geologic mapping of surface ruptures indicative of shear zones in alluvium due to the Landers earthquake shows a maximum length of shear fractures to be of the order of 500 m [e.g., *Johnson et al.*, 1994; *Sowers et al.*, 1994].

The fractures between the rupture on the Camp Rock-Emerson Faults and the Johnson Valley Fault are similar in style to fracture patterns seen in much smaller versions of shear zones associated with the Landers earthquake [e.g., *Johnson et al.*, 1994]. As the orientation of a fracture changes with respect to the look direction of the radar, the sense of slip on a fracture with the same phase gradient sign changes. Hence the smaller fractures close to the Johnson Valley Fault (Plate 3c) most likely

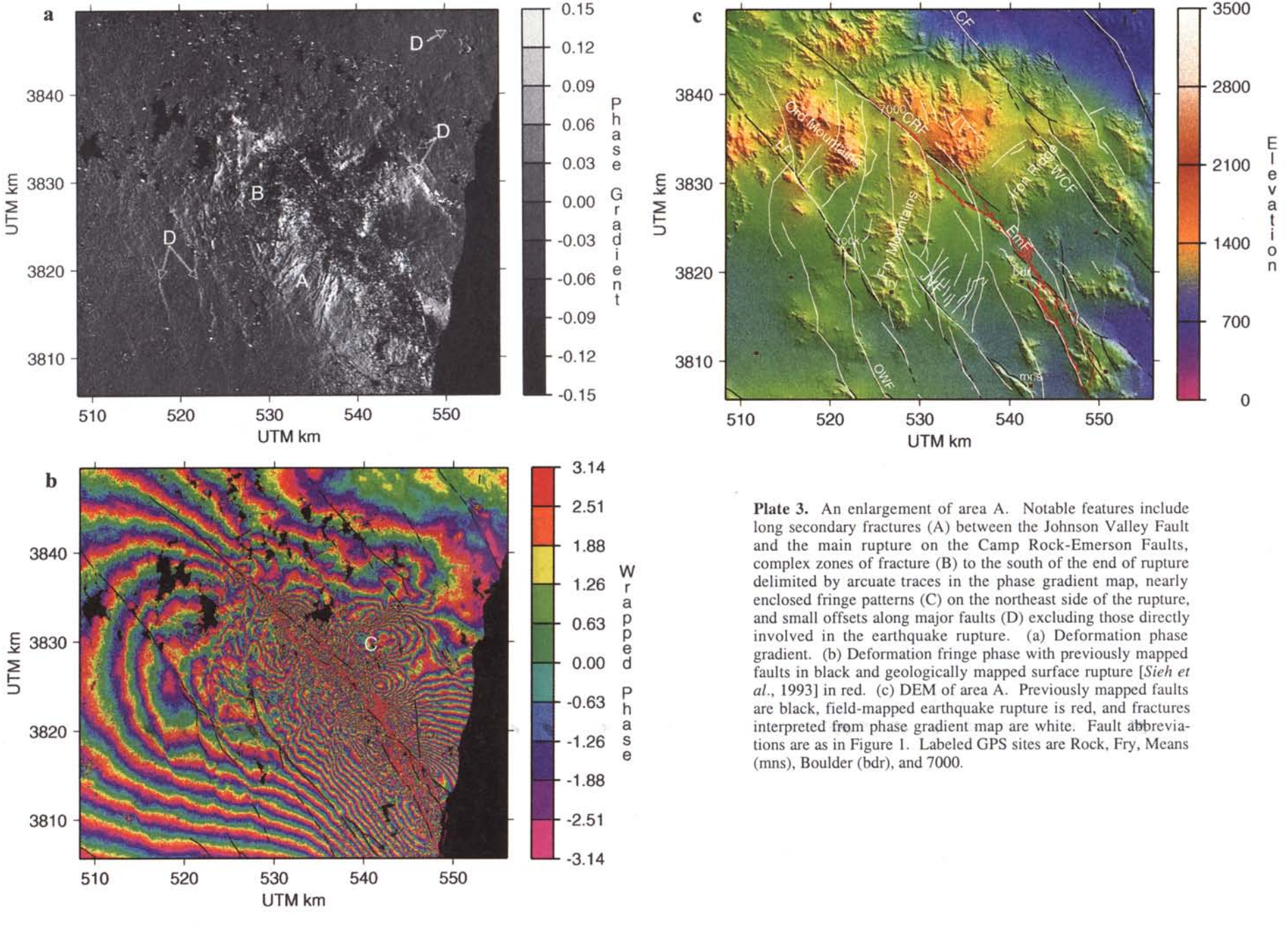

Plate 3. An enlargement of area A. Notable features include long secondary fractures (A) between the Johnson Valley Fault and the main rupture on the Camp Rock-Emerson Faults, complex zones of fracture (B) to the south of the end of rupture delimited by arcuate traces in the phase gradient map, nearly enclosed fringe patterns (C) on the northeast side of the rupture, and small offsets along major faults (D) excluding those directly involved in the earthquake rupture. (a) Deformation phase gradient. (b) Deformation fringe phase with previously mapped faults in black and geologically mapped surface rupture [*Sieh et al.*, 1993] in red. (c) DEM of area A. Previously mapped faults are black, field-mapped earthquake rupture is red, and fractures interpreted from phase gradient map are white. Fault abbreviations are as in Figure 1. Labeled GPS sites are Rock, Fry, Means (mns), Boulder (bdr), and 7000.

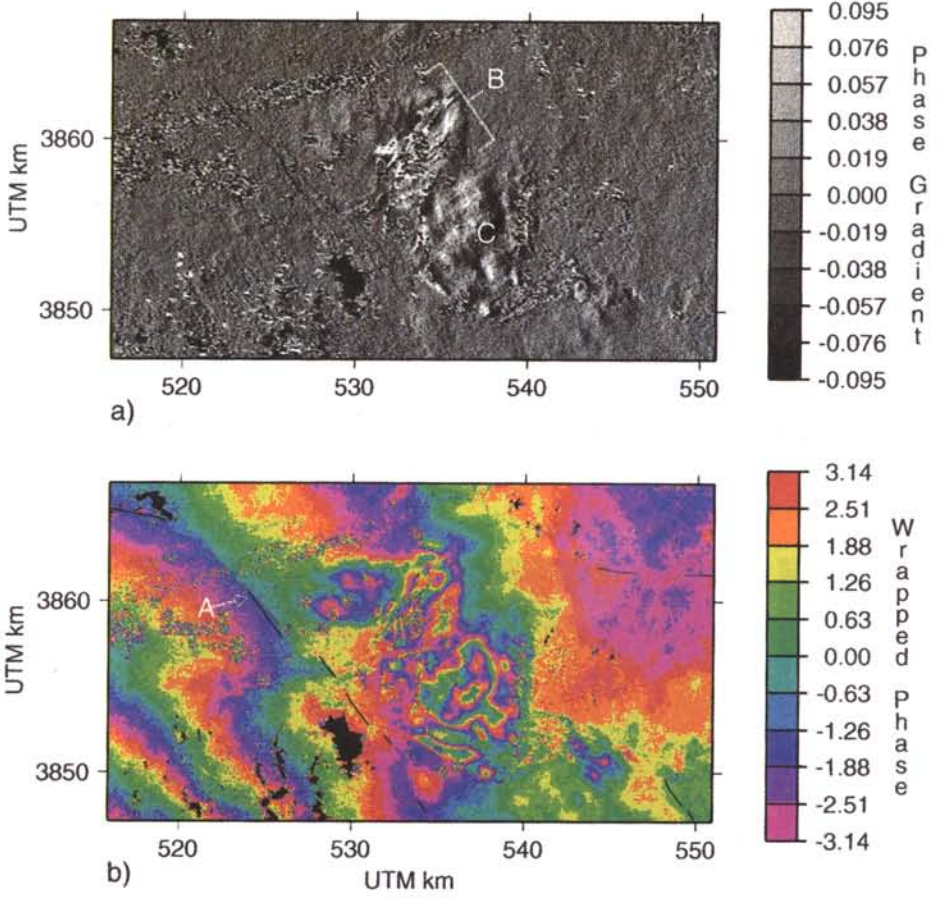

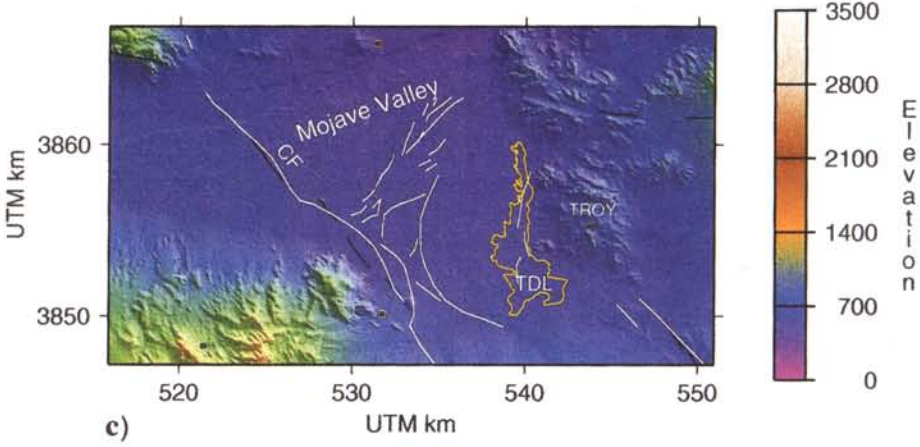

Plate 4. An enlargement of area B. Notable features are offsets along major faults, and a zone of fracturing, flanked by two zones of enclosed fringe patterns, in the center. The Calico Fault (A) runs through the left half. The Newberry fractures (B) and Troy Dry Lake (C) are located in the center. (a) Deformation phase gradient. (b) Deformation fringe phase. Black lines are previously mapped faults. (c) DEM of area B. Previously mapped faults are black, fractures interpreted from phase gradient map are white, and outline of Troy Dry Lake (TDL) is yellow. GPS site TROY is marked.

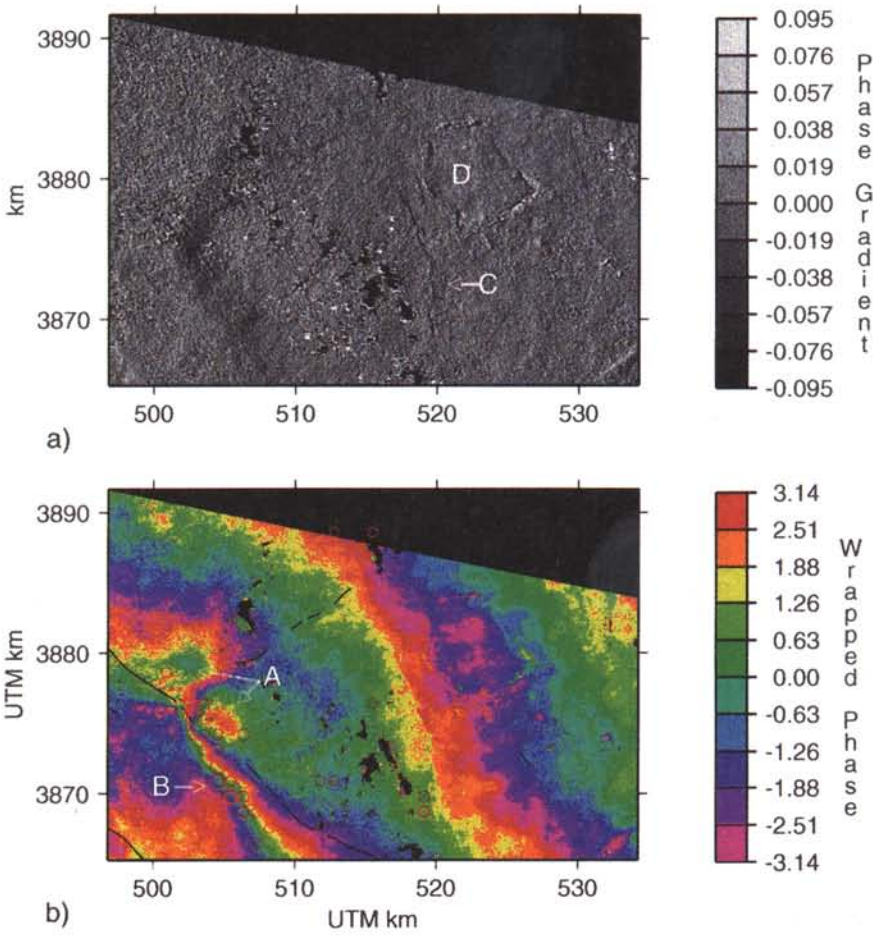

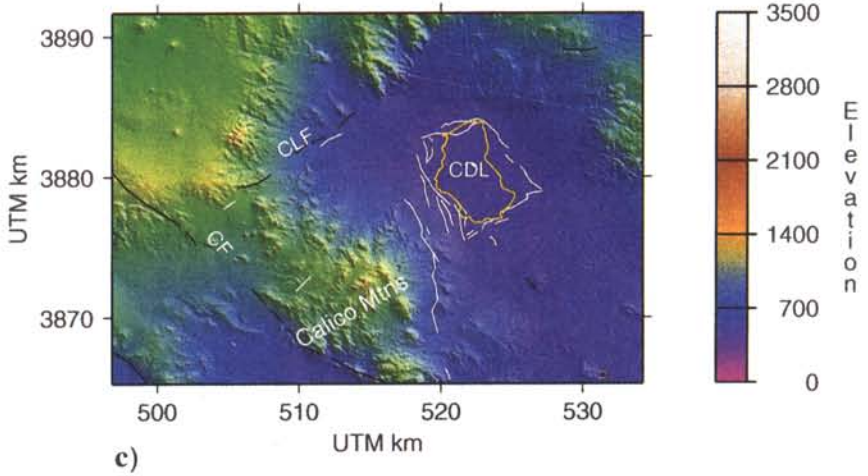

Plate 5. An enlargement of area C. The enclosed fringes labeled "A" indicate deformation related to the intersection of the Barstow Cluster and preexisting faults. A northern branch of the Calico Fault (C) and some deformation around the shoreline of Coyote Dry Lake (D) are apparent in the phase gradient image. (a) Deformation phase gradient. (b) Deformation fringe phase with faults in black and shocks in red. (c) DEM of area C. Previously mapped faults are black, fractures interpreted from phase gradient map are white, and outline of Coyote Dry Lake (CDL) is yellow.

have left-lateral offsets across them, while the larger fractures that traverse the entire valley floor to intersect with the main rupture most likely accomodate left-lateral offsets near the Johnson Valley Fault which change to right-lateral offsets as the fractures near the main rupture. This behavior is similar to that of a curved fracture in the Happy Trail shear zone observed by *Johnson et al.* [1994]. The fracture flanking the eastern side of the Fry Mountains (Plate 3c) probably also accommodated some east-side-up motion similar to some fractures seen in the Happy Trail shear zone. Because of their regular spacing between mountain ranges, the long fractures in the Johnson Valley and between the Lenwood Fault and the northwestward continuation of the earthquake rupture may be related to and/or facilitate the uplift of the Fry and Ord Mountains (Plate 3c).

The fractures in the upper Johnson Valley may have collectively accommodated some significant portion of right-lateral shear. *Murray et al.* [1993] require ~0.5 m of right-lateral slip on a northwest trending fault between stations Boulder and Means on the east and Old Woman, Fry, and Rock on the west (Plate 3c) to fit their trilateration data to an elastic half-space model. The tie lines between the above stations span the upper Johnson Valley. Because displacement on the upper Johnson Valley Fault (which runs through the upper Johnson Valley between the Johnson Valley Fault and the Camp Rock-Emerson Faults) was of the order of centimeters (K. LaJoie, personal communication, 1997), offset on another fault or over a region is necessary to fit the geodetic data. This discrepancy could be resolved with further modeling of the displacement expected from an elastically responding lithosphere and comparison of models to interferometric results.

Stress changes on faults not involved in the main rupture are indicated by published and preliminary modeling of the stress field induced by the earthquake in an elastic half-space [*Harris and Simpson*, 1992; *Stein et al.*, 1992; R. Simpson, personal communication, 1997]. Two lines of evidence suggest that InSAR observed displacements on the Lenwood and Old Woman Faults were vertical, west-side-up rather than left-lateral and sympathetic. First, Coulomb failure stress is predicted to have decreased by only as much as 17 bars across the Lenwood and northern portion of the Old Woman Fault [*Harris and Simpson*, 1992], while the calculated stress drop on the Landers earthquake surface rupture was ~85 bars; assuming that the level of stress on other faults in the Mojave Desert before the earthquake was similar to that on the faults involved in the Landers earthquake, a 17-bar stress drop would not be enough to induce sympathetic slip. Second, preliminary modeling results show vertical displacements across these faults, if present, should be west-side-up (R. Simpson, internet communication, 1997). Thus, while the Lenwood and northern Old Woman Faults probably relaxed subsequent to the Landers earthquake, the stress drop was not enough to induce left-lateral, sympathetic slip. Instead, the displacements measured in the SAR interferogram were probably vertical, west-side-up which is consistent with the geomorphology (Plate 1).

Geologic field mapping and tectonic modeling suggest that the offset observed by InSAR on the Calico Fault was right-lateral. The Calico Fault (Figure 6) lies in a region of the model of *Stein et al.* [1992] in which faults on optimally oriented planes were brought closer to failure by the Landers earthquake-induced stress field. Geologic mapping indicates right-lateral slip on the Calico Fault [*Hart et al.*, 1993]. Also, there are no geomorphic structures directly related to the Calico Fault that would indicate that it accommodates vertical motions (Plate 4c).

The Newberry fractures were mapped by geologists [*Unruh et al.*, 1994; K. LaJoie, personal communication, 1998] immediately after the Landers earthquake. The *Unruh et al.* [1994] study shows a series of parallel, linear fractures trending N-NE, while more detailed mapping by K. LaJoie in the field and using air photographs shows curved fractures similar to those seen in the SAR interferogram (Plates 4a and 4c). These fractures opened preexisting structures and exhibited normal dip-slip separation of as much as 12 cm and lateral offsets of 5 cm or less [*Unruh et al.*, 1994]. These structures are interpreted by *Unruh et al.* [1994] as evidence of pure northwest-southeast extension. The collocation of these fractures with extensional basins may show how, incrementally, the Troy Dry Lake bed was formed or may be related to internal deformation of the lake bed itself. The region surrounding the Newberry fractures and Calico Fault shows a deviation from the fringe pattern expected from modeling an elastic lithosphere's response to the earthquake [e.g., *Massonnet et al.*, 1993]. This deviation could be due to inhomogeneities in the crust and may account for some of the anomalous motion at Mojave GPS network station TROY (Plate 4c) where motion was 150% of that expected from elastic half-space models [*Miller et al.*, 1993].

Deformation near the Calico Fault related to the Barstow earthquake cluster is a further example of small-scale deformation associated with the Landers earthquake-induced stress field. Earthquakes of the Barstow Cluster were confined to depths less than 10 km and occurred along a linear trend not related to any geologically mapped fault. The Barstow shocks began 6-8 hours after the Landers main shock [*Hauksson et al.*, 1993]. In the interferogram (Plate 5b), the only clear fringe pattern associated with the Barstow Cluster occurs where its trend intersects the Calico and Coyote Faults. However, there is negative shading in the phase gradient map aligned with the cluster (Plate 5a) that indicates diffuse right-lateral shear likely related to faulting at depth. The enclosed fringe patterns at the intersection of the Calico and Coyote Lake Faults (Plate 5b) are probably indicative of uplift of the Calico Mountains on the southeast side of the Coyote Lake Fault and subsidence on the northwest side of the Coyote Lake Fault as the Calico Fault accommodated a right-lateral offset.

Because GPS results adequately fit far-field coseismic displacements as predicted by an elastic half-space model [*Bock et al.*, 1993; *Blewitt et al.*, 1993], such a model can be presumed to be a good one for the large-scale displacement pattern associated with the earthquake rupture. Small-scale anomalies in the displacement field are most likely confined to the region within 100 km of the earthquake rupture and are likely due to interaction of crustal and surficial structures with the earthquake induced stress field. These small-scale anomalies could account for some of the deviation from an elastic half-space model in the near-field such as noted by *Miller et al.* [1993], *Murray et al.* [1993], and *Hudnut et al.* [1994].

It is unfortunate that more detailed field observations of the Landers earthquake rupture are not available to ground truth InSAR observations. Air photographs show offsets along some fractures that corroborate InSAR observations (Newberry fractures) but do not exhibit fine details such as seen in the upper Johnson Valley region of the interferogram (K. LaJoie, personal communication, 1997). If InSAR observations including the displacement field and displacement phase gradient were made available within a few months of the earthquake, it might have been possible to plan field surveys to study features seen in the interferogram. Our own expedition into the field (January 1997)

indicated that much of the millimeter and centimeter scale deformation has been eroded by natural processes and recreational vehicles.

6. Conclusions

SAR interferometry allows near total spatial coverage of the radar LOS deformation and the gradient of the radar LOS deformation in the region of a major earthquake. This spatial coverage allows us to study heterogeneity in the deformation field. This heterogeneity can be investigated using the phase gradient map which highlights offsets on major faults, secondary fractures, and geologic structures that are not apparent in interferogram fringe maps. Interpretations of these interferogram fringe and phase gradient maps depend on ancillary information including geological field mapping, GPS measurements, and lithospheric modeling to determine meaningful displacements on and across geological structures.

Our observations show that there is localized heterogeneity in the deformation field of the Landers earthquake within 80-100 km of the main rupture. Unmapped faults or questionable extensions of previously mapped faults which experienced triggered slip are highlighted by the phase gradient observations. Secondary fractures in the upper Johnson Valley indicate a shear zone between the Johnson Valley Fault and the main rupture that may include the region between the Lenwood Fault and the Camp Rock Fault occupied by the Fry and Ord Mountains. Previously mapped fractures associated with extension in the Mojave Valley are apparent in the phase gradient map and corroborate field observations. Also, there are correlations between fringe patterns and geomorphology indicating incremental deformation of extensional and compressional structures including Iron Ridge, the Calico Mountains, Coyote Dry Lake, and Troy Dry Lake.

Appendix A: Interferometer Geometry and Equations

If λ is the wavelength of the radar and $\delta\rho$ is the range difference between the reference and repeat passes of the satellite, the interferogram phase of a point on the ground is $\phi = (4\pi/\lambda)\delta\rho$. We present the interferometer geometry and range difference attributable to three factors: (1) spheroidal Earth with no topography, (2) topography, and (3) surface deformation. We use these relationships to show how the phase gradient of interferograms may be scaled so that phase gradients of interferograms with different baselines may be added to and subtracted from each other.

A1. Range Difference Due to Spheroidal Earth

The relationship between the repeat-pass range to an Earth with no topography or surface deformation ($\rho + \delta\rho_e$), the reference-pass range (ρ), the baseline length (B), and the baseline elevation angle (α) is provided by the law of cosines [Zebker et al., 1994] (Figure A1). Applying the parallel ray approximation [Zebker and Goldstein, 1986], the range difference is

$$\delta\rho_e = -B\sin(\theta_0 - \alpha) \tag{A1}$$

where θ_0 is the look angle to a spheroidal Earth defined by $\cos\theta_0 = (c^2 + \rho^2 - r^2)/2\rho c$, where c is the distance from the center of the Earth to the location of the satellite reference pass and r is the distance from the center of the Earth to the location on the Earth that is illuminated when the range from the satellite to the Earth is ρ.

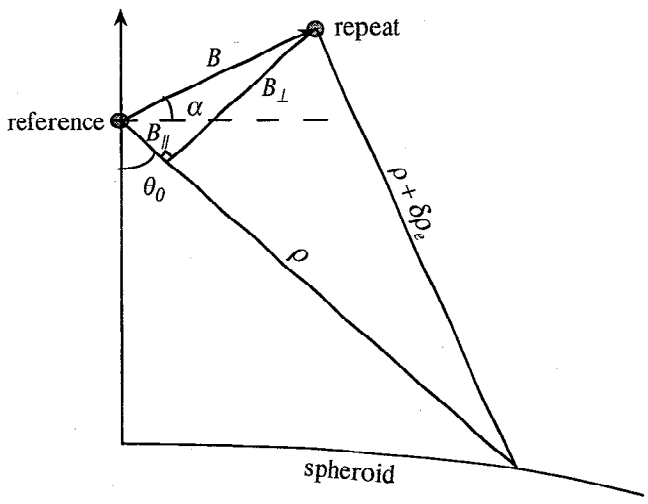

Figure A1. InSAR geometry for spheroidal Earth with no topography or surface deformation. Here ρ is range from the "reference" satellite pass to a location on the spheroid, $\rho+\delta\rho_e$ is range from the "repeat" satellite pass to the same location, θ_0 is the radar look angle, α is the baseline elevation angle, B is the baseline length, $B_\parallel$ is the component of the baseline parallel to the satellite reference pass line of site, and $B_\perp$ is the component of the baseline perpendicular to the satellite reference pass line of site.

We define the components of the baseline parallel ($B_\parallel$) and perpendicular ($B_\perp$) to the range ray referenced to a spheroidal Earth as

$$B_\parallel = B\sin(\theta_0 - \alpha) \tag{A2a}$$

$$B_\perp = B\cos(\theta_0 - \alpha) \tag{A2b}$$

The range difference due to a spheroidal Earth with no topography is equal to the parallel component of the baseline.

A2. Range Difference Due to Topography on a Spheroidal Earth

Here the range difference ($\delta\rho_e + \delta\rho_t$) is influenced by the topography (see Figure A2) so that

$$\delta\rho_e + \delta\rho_t = -B\sin(\theta_0 + \delta\theta_t - \alpha) \tag{A3}$$

where θ is the angle between the vertical and the reference pass range ray and is the sum of two terms: θ_0 is the look angle for a spheroidal Earth with no topography and $\delta\theta_t$ is the angular distortion caused by the presence of topography.

Since the spacecraft is far from the Earth, $\delta\theta_t$ is small and the range difference due to topography on a spheroidal Earth ($\delta\rho_e + \delta\rho_t$) is

$$\delta\rho_e + \delta\rho_t = -(B_\parallel + \delta\theta_t B_\perp) \tag{A4}$$

We perform the "flat Earth" correction by computing $B_\parallel$ using equation (A1) and removing it from the interferogram phase.

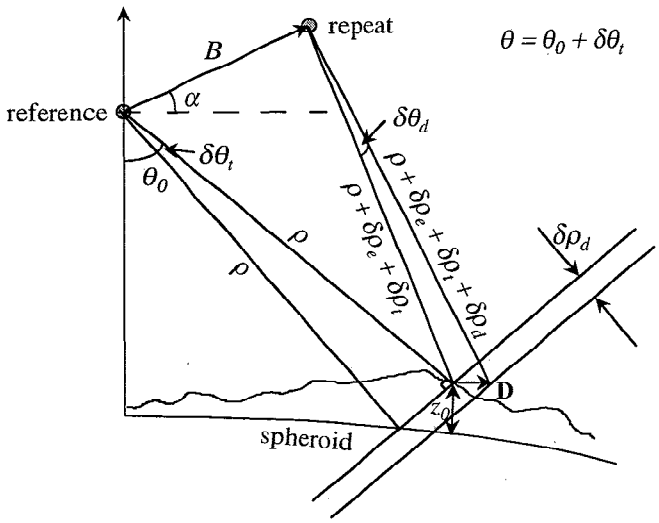

Figure A2. InSAR geometry for spheroidal Earth with topography and surface deformation. Here ρ is range from the "reference" satellite pass to a location on the surface of the Earth at elevation z_0, $\rho + \delta\rho_e + \delta\rho_t$ is range from the "repeat" satellite pass to the same location, $\rho + \delta\rho_e + \delta\rho_t + \delta\rho_d$ is the range from the repeat pass of the satellite to the same piece of Earth after is has been displaced by **D**, θ_0 is the radar look angle to the reference spheroid for range ρ, $\delta\theta_t$ is the topographic angular distortion, $\delta\theta_d$ is the displacement angular distortion, α is the baseline elevation angle, and B is the baseline length. When measuring deformations using space-based InSAR, the three range rays (excluding the one drawn to the reference spheroid) in the figure can be considered parallel to each other making $\delta\theta_d$ essentially zero. The InSAR measured component of the displacement, **D**, is that which is in the direction of the satellite LOS. This displacement is equal to $\delta\rho_d$.

A3. Range Difference for Topography and Deformation on a Spheroidal Earth

By inspecting Figure A2 and making several assumptions, one comes to the conclusion that a displacement vector is projected into the satellite line-of-sight direction and it contributes additively to the range change due to topography and a spheroidal Earth. Because the spacecraft is far from the Earth (800 km), it can be assumed that the ray with length ρ is parallel to the ray with length $\rho + \delta\rho_e + \delta\rho_t$ and the ray with length $\rho + \delta\rho_e + \delta\rho_t + \delta\rho_d$. Implicit in this assumption is that $\delta\theta_d$ is essentially zero and the radar signal wavefronts are perpendicular to the above rays. Now, the range difference is

$$\delta\rho = \delta\rho_e + \delta\rho_t + \delta\rho_d = -(B_{\parallel} + \delta\theta_t B_{\perp} - \delta\rho_d) \tag{A5}$$

To isolate the range change due to deformation, we remove the flat Earth range change (see above) and the topographic range change estimated from other interferograms (see below).

A4. Scale Factors for Interferograms Which Have Had the Flat Earth Correction Applied

Consider two interferograms which have both had the flat Earth correction applied. Interferogram 1 (ϕ_1) has phase due only to topographic angular distortion and interferogram 2 (ϕ_2) has phase due to topographic angular distortion and displacement. If the interferograms are matched to the same reference geometry, the topographic angular distortion is assumed to be the same for both and interferogram 1 can be scaled by the ratio of the perpendicular baselines and subtracted from interferogram 2 to yield the displacement in the satellite LOS [*Zebker et al.*, 1994]:

$$\phi_2 - \frac{B'_{\perp}}{B_{\perp}}\phi_1 = \frac{4\pi}{\lambda}\delta\rho_d \tag{A6}$$

where $B_{\perp}$ is the perpendicular component of the baseline for interferogram 1 and $B_{\perp}'$ is the perpendicular component of the baseline for interferogram 2.

The interferogram scale factor (see equation (6)) is the ratio of the perpendicular baselines of each starting interferogram. This scale factor can be applied directly to the interferogram phase gradient (in range) to extract the interferogram deformation phase gradient, $4\pi/\lambda(\partial\delta\rho_d/\delta\rho)$, using

$$\frac{\partial\phi_2}{\partial\rho} - \frac{B'_{\perp}}{B_{\perp}}\frac{\partial\phi_1}{\partial\rho} = \frac{4\pi}{\lambda}\frac{\partial\delta\rho_d}{\partial\rho} \tag{A7}$$

The LOS displacement gradient, $\partial D_{LOS}/\partial\rho$, is then equal to the deformation range-difference gradient, $\partial\delta\rho_d/\partial\rho$.

Appendix B: Low-Pass and Gradient Filters

Interferograms formed from full-resolution, SAR images contain significant phase noise. The gradient operation amplifies the shortest-wavelength noise resulting in a noisy estimate of phase gradient. To suppress a portion of this noise, we filter the data before computing the gradient by forming a multilook average using a Gaussian-shaped filter. We have designed a convolution filter that is nearly isotropic in ground range/azimuth space consistent with the sampling frequency of the radar:

$$f(x,y) = \exp\left[\frac{x^2 + y^2}{2\sigma^2}\right] \tag{B1}$$

where x is range, y is azimuth, and σ is filter width. Based on visual inspection of a variety of interferograms, we have chosen σ = 8 m so that 0.5 gain occurs at a wavelength of 42 km in slant range (~107 m in ground range) and 84 m in azimuth. Based on a cross-spectral analysis of repeat tandem interferograms [*Sandwell and Price*, 1997], we found signal-to-noise ratios of 1 at a wavelength of 230 m in ground range and 180 m in azimuth. Thus the low-pass Gaussian is passing all of the relevant signals.

The gradient operation follows the low-pass Gaussian filter. We have designed a derivative filter using the Parks-McClellan approach. The filter coefficients and imaginary response are shown in Figure B1. The derivative filter is 17 points long (solid curve, Figure B1a), while the Gaussian filter is only 5 points long in range (dashed). Figure B1b shows the gain for a theoretical derivative (dotted) and the numerical derivative (solid). The convolution of the Gaussian and derivative filters (dashed) has a peak response at a wavelength of 50 m. The location of the peak can be adjusted by varying σ in equation (B1), although the derivative filter limits the best resolution to 30 m wavelength.

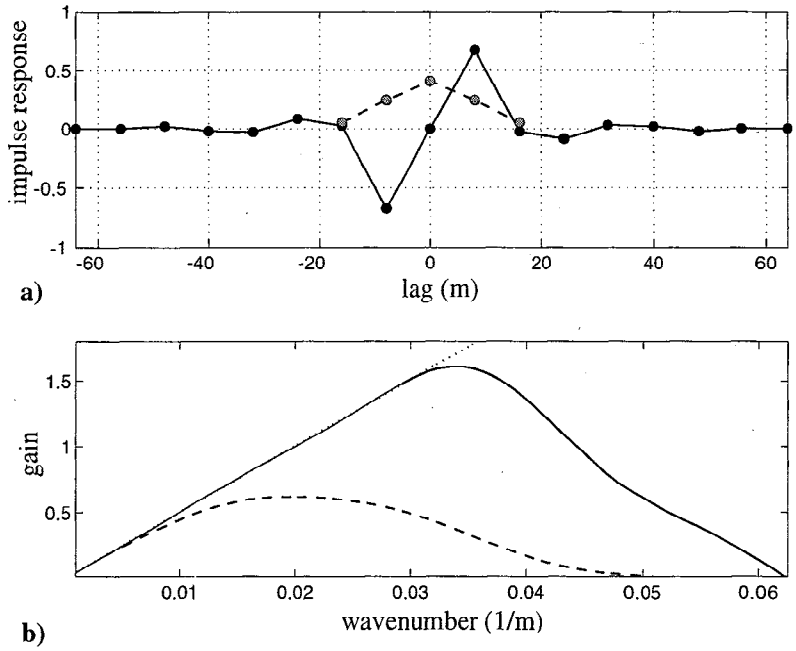

Figure B1. (a) Filters used in interferogram phase gradient formation. Solid line is the gradient filter, dashed line is the smoothing filter. (b) Gain for theoretical derivative filter (dotted line), numerical derivative filter (solid line), and the convolution of the Gaussian smoothing and numerical derivative filters (dashed line).

Acknowledgments. We thank Howard Zebker for help developing an InSAR processing system and for providing us with some of the algorithms used to process our data. Duncan Agnew suggested we formalize the relationship between the phase gradient and the deformation gradient tensor and pointed us toward important geodetic observations pertinent to this work. We thank Ken LaJoie and Bob Simpson for discussions aiding in the interpretation of the data. We thank Bernard Minster for a careful and constructive internal review. Finally, we thank Paul Rosen and Howard Zebker for helpful external reviews. This research was supported by NASA (HPCC/ESS and SENH Programs) and NSF (EAR-19201). Evelyn Price was supported as a SIO/NASA/ Goddard JCOSS student fellow.

References

Blewitt, G., M.B. Heflin, K.J. Hurst, D.C. Jefferson, F.H. Webb, and J.F. Zumberge, Absolute far-field displacements from the 28 June 1992 Landers earthquake sequence, *Nature, 361*, 340-342, 1993.

Bock, Y., et al, Detection of crustal deformation from the Landers earthquake sequence using continuous geodetic measurements, *Nature, 361*, 337-340, 1993.

Carter, J.N., B.P. Luyendyk, and R.R. Terres, Neogene clockwise rotation of the eastern Transverse Ranges, California, suggested by paleomagnetic vectors, *Geol. Soc. Am. Bull., 98*, 199-206, 1987.

Curlander, J.C., and R.N. McDonough, *Synthetic Aperture Radar: Systems and Signal Processing*, edited by J.A. Kong, John Wiley, New York, 1991.

Dibblee, T.W., Geologic map of the Rodman Mountains quadrangle, San Bernardino County, California, *U.S. Geol. Surv. Publ., I-430*, 1964.

Dokka, R.K., and C.J. Travis, Late Cenozoic strike-slip faulting in the Mojave Desert, California, *Tectonics, 9*, 311-340, 1990a.

Dokka, R.K., and C.J. Travis, Role of the eastern California shear zone in accommodating Pacific-North American plate motion, *Geophys. Res. Lett., 17*, 1323-1326, 1990b.

Doser, D.I., A re-examination of the 1947 Manix, California, earthquake sequence and comparison to other sequences within the Mojave Block, *Bull. Seismol. Soc. Am., 80*, 267-277, 1990.

Feigl, K.L., A. Sergent, and D. Jacq, Estimation of an earthquake focal mechanism from a satellite radar interferogram: Application to the December 4, 1992 Landers aftershock, *Geophys. Res. Lett., 22*, 1037-1040, 1995.

Fuis, G.S., and A.G. Lindh, A change in fault-plane orientation between foreshocks and aftershocks of the Galway Lake earthquake, $M_l = 5.2$, 1975, Mojave Desert, California, *Tectonophysics, 52*, 601-602, 1979.

Gabriel, A.K., and R.M. Goldstein, Crossed orbit interferometry: Theory and experimental results from SIR-B, *Int. J. Remote Sens., 9*, 857-872, 1988.

Gabriel, A.K., R.M. Goldstein, and H.A. Zebker, Mapping small elevation changes over large areas: Differential radar interferometry, *J. Geophys. Res., 94*, 9183-9191, 1989.

Garfunkel, Z., Model for the late Cenozoic tectonic history of the Mojave Desert and its relation to adjacent areas, *Geol. Soc. Am. Bull., 85*, 1931-1944, 1974.

Goldstein, R.M., Atmospheric limitations to repeat-track radar interferometry, *Geophys. Res. Lett., 22*, 2517-2520, 1995.

Goldstein, R.M., H.A. Zebker, and C.L. Werner, Satellite radar interferometry: Two-dimensional phase unwrapping, *Radio Sci., 23*, 713-720, 1988.

Graham, L.C., Synthetic interferometer radar for topographic mapping, *Proc. IEEE, 62*, 763-768, 1974.

Harris, R.A., and R.W. Simpson, Changes in static stress on southern California faults after the 1992 Landers earthquake, *Nature, 360*, 251-254, 1992.

Hart, E.W., W.A. Bryant, and J.A. Treiman, Surface faulting associated with the June 1992 Landers earthquake, California, *Calif. Geol., 46*, 10-16, 1993.

Hauksson, E., State of stress from focal mechanisms before and after the 1992 Landers earthquake sequence, *Bull. Seismol. Soc. Am., 84*, 917-934, 1994.

Hauksson, E., L.M. Jones, K. Hutton, and D. Eberhart-Phillips, The 1992 Landers earthquake sequence: Seismological observations, *J. Geophys. Res., 98*, 19,835-19,858, 1993.

Hill, R.L., and D.J. Beeby, Surface faulting associated with the 5.2 magnitude Galway Lake earthquake of May 31, 1975: Mojave Desert, San Bernardino County, California, *Geol. Soc. Am. Bull., 88*, 1378-1384, 1977.

Hill, R.L., J.A. Treiman, and J.W. Given, Geologic Study of the Homestead Valley Earthquake Swarm of March 15, 1979, *California Geology*, 60-67, 1980.

Hudnut, K.W., et al., Co-seismic displacements of the 1992 Landers earthquake sequence, *Bull. Seismol. Soc. Am., 84*, 625-645, 1994.

Johnson, A.M., R.W. Fleming, and K.M. Cruikshank, Shear zones formed along long straight traces of fault zones during the 28 June 1992

Landers, California, earthquake, *Bull. Seismol. Soc. Am., 84*, 499-510, 1994.

Kanamori, H., H.K. Thio, D. Dreger, E. Hauksson, and T. Heaton, Initial investigation of the Landers, California earthquake of 28 June 1992 using TERRAscope, *Geophys. Res. Lett., 19*, 2267-2270, 1992.

Li, F.K., and R.M. Goldstein, Studies of multibaseline spaceborne interferometric synthetic aperture radars, *IEEE Trans. Geosci. Remote Sens., 28*, 88-97, 1990.

Malvern, L.E., *Introduction to the Mechanics of a Continuous Medium*, Prentice-Hall, Englewood Cliffs, N.J., 1969.

Massonnet, D., and K.L. Feigl, Discrimination of geophysical phenomena in satellite radar interferograms, *Geophys. Res. Lett., 22*, 1537-1540, 1995a.

Massonnet, D., and K.L. Feigl, Satellite radar interferometric map of the coseismic deformation field of the $M = 6.1$ Eureka Valley, California earthquake of May 17, 1993, *Geophys. Res. Lett., 22*, 1541-1544, 1995b.

Massonnet, D., M. Rossi, C. Carmona, F. Adragna, G. Peltzer, K. Feigl, and T. Rabaute, The displacement field of the Landers earthquake mapped by radar interferometry, *Nature, 364*, 138-142, 1993.

Massonnet, D., K. Feigl, M. Rossi, and F. Adragna, Radar interferometric mapping of deformation in the year after the Landers earthquake, *Nature, 369*, 227-230, 1994.

McDonough, R.N., B.E. Raff, and J.L. Kerr, Image formation from spaceborne synthetic aperture radar signals, *Johns Hopkins APL Tech. Dig., 6*, 300-312, 1985.

Miller, M.M., F.H. Webb, D. Townsend, M.P. Golombek, and R.K. Dokka, Regional coseismic deformation from the June 28, 1992, Landers, California, earthquake: Results from the Mojave GPS network, *Geology, 21*, 868-872, 1993.

Murray, M.H., J.C. Savage, M. Lisowski, and W.K. Gross, Coseismic displacements: 1992 Landers, California, earthquake, *Geophys. Res. Lett., 20*, 623-626, 1993.

Peltzer, G., K.W. Hudnut, and K.L. Feigl, Analysis of coseismic surface displacement gradients using radar interferometry: New insights into the Landers earthquake, *J. Geophys. Res., 99*, 21,971-21,981, 1994.

Peltzer, G., P. Rosen, F. Rogez, and K. Hudnut, Postseismic rebound in fault step-overs caused by pore fluid flow, *Science, 273*, 1202-1204, 1996.

Richter, C.F., The Manix (California) earthquake of April 20, 1947, *Bull. Seismol. Soc. Am., 37*, 171-179, 1947.

Rosen, P.A., S. Hensley, H.A. Zebker, F.H. Webb, and E. Fielding, Surface deformation and coherence measurements of Kilauea Volcano, Hawaii from SIR-C radar interferometry, *J. Geophys. Res., 101*, 23,109-23,125, 1996.

Sandwell and Price, Sums and Differences of Interferograms, *Eos Trans. AGU*, 78(46), Fall Meet. Suppl., F144, 1997.

Sauber, J., W. Thatcher, and S.C. Solomon, Geodetic measurement of deformation in the central Mojave Desert, California, *J. Geophys. Res., 91*, 12,683-12,693, 1986.

Savage, J.C., M. Lisowski, and W.H. Prescott, An apparent shear zone trending north-northwest across the Mojave Desert into Owens Valley, eastern California, *Geophys. Res. Lett., 17*, 2113-2116, 1990.

Scharoo, R., and P.N.A.M. Visser, Precise orbit determination and gravity field improvement for the ERS satellites, *J. Geophys. Res., 103*, 8113-8127, 1998.

Sieh, K., et al., Near-field investigations of the Landers earthquake sequence, April to July 1992, *Science, 260*, 171-176, 1993.

Sowers, J.M., J.R. Unruh, W. R. Lettis, and T.D. Rubin, Relationship of the Kickapoo Fault to the Johnson Valley and Homestead Valley Faults, San Bernardino County, California, *Bull. Seismol. Soc. Am., 84*, 528-536, 1994.

Stein, R.S., G.C.P. King, and J. Lin, Change in failure stress on the southern San Andreas fault system caused by the 1992 magnitude = 7.4 Landers earthquake, *Science, 258*, 1328-1332, 1992.

Tarayre, J., and D. Massonnet, Atmospheric propagation heterogeneities revealed by ERS-1 interferometry, *Geophys. Res. Lett., 23*, 989-992, 1996.

Unruh, J.R., W.R. Lettis, and J.M. Sowers, Kinematic interpretation of the 1992 Landers earthquake, *Bull. Seismol. Soc. Am., 84*, 537-546, 1994.

Werner, C.L., S. Hensley, R.M. Goldstein, P.A. Rosen, and H.A. Zebker, Techniques and applications of SAR interferometry for ERS-1: Topographic mapping, change detection, and slope measurement, *First ERS-1 Symposium – Space at the Service of our Environment*, Cannes, France, 205-210, 1992.

Wesnousky, S.G., Earthquakes, Quaternary Faults, and Seismic Hazard in California, *J. Geophys. Res., 91*, 12,587-12,631, 1986.

Zebker, H.A., and R.M. Goldstein, Topographic mapping from interferometric synthetic aperture radar observations, *J. Geophys. Res., 91*, 4993-4999, 1986.

Zebker, H.A., and J. Villasenor, Decorrelation in interferometric radar echoes, *IEEE Trans. Geosci. Remote Sens., 30*, 950-959, 1992.

Zebker, H.A., P.A. Rosen, R.M. Goldstein, A. Gabriel, and C.L. Werner, On the derivation of coseismic displacement fields using differential radar interferometry: The Landers earthquake, *J. Geophys. Res., 99*, 19,617-19,643, 1994.

Zebker, H.A., P.A. Rosen, and S. Hensley, Atmospheric effects in interferometric synthetic aperture radar surface deformation and topographic maps, *J. Geophys. Res., 102*, 7547-7563, 1997.

E.J. Price and D.T. Sandwell, IGPP 0225, Scripps Institution of Oceanography, University of California, San Diego, La Jolla, CA 92093-0225. (e-mail: evelyn@seasat.ucsd.edu; sandwell@gcosat.ucsd.edu)

(Received September 19, 1997; revised May 6, 1998;
accepted May 22, 1998.)